INTERNATIONAL JOURNAL FOR NUMERICAL METHODS IN FLUIDS
Int. J. Numer. Meth. Fluids 2004; **44**:331–346 (DOI: 10.1002/fld.643)

Numerical simulation on an interaction of a vortex street with an elliptical leading edge using an unstructured grid

Sangmook Shin[1,*,†], Chan Ki Kim[1] and Kwang June Bai[2]

[1]*Agency for Defense Development, Jinhae, Korea*
[2]*Department of Naval Architecture and Ocean Engineering, Seoul National University, Seoul, Korea*

SUMMARY

An algorithm for a time accurate incompressible Navier–Stokes solver on an unstructured grid is presented. The algorithm uses a second order, three-point, backward difference formula for the physical time marching. For each time step, a divergence free flow field is obtained based on an artificial compressibility method. An implicit method with a local time step is used to accelerate the convergence for the pseudotime iteration. To validate the code, an unsteady laminar flow over a circular cylinder at a Reynolds number of 200 is calculated. The results are compared with available experimental and numerical data and good agreements are achieved.

Using the developed unsteady code, an interaction of a Karman vortex street with an elliptical leading edge is simulated. The incident Karman vortex street is generated by a circular cylinder located upstream. A clustering to the path of the vortices is achieved easily due to flexibility of an unstructured grid. Details of the interaction mechanism are analysed by investigating evolutions of vortices. Characteristics of the interactions are compared for large- and small-scale vortex streets. Different patterns of the interaction are observed for those two vortex streets and the observation is in agreement with experiment. Copyright © 2004 John Wiley & Sons, Ltd.

KEY WORDS: unstructured grid; time accurate incompressible Navier–Stokes solver; artificial compressibility; vortex street interaction

1. INTRODUCTION

There are two main types for time accurate incompressible Navier–Stokes solvers. One is based on the projection method in which pressure field at each time step is calculated from a Poisson equation [1]. The other is based on the artificial compressibility method with a pseudotime subiteration [2]. In this study, the artificial compressibility method is adapted and the convergence for the pseudotime iteration is accelerated using an implicit method with a local time stepping. The augmentation with the artificial compressibility makes it possible to

*Correspondence to: Sangmook Shin, Hydrodynamic Modeling & Simulation, 2nd Research and Development Center, Agency for Defense Development, P.O. Box 18, 645-600 Jinhae, Korea.
†E-mail: smshin@add.re.kr

Received 26 November 2002
Revised 3 September 2003

use several schemes that are developed for general hyperbolic type conservation laws such as the flux splitting method for inviscid flux calculation. Roe's flux difference splitting method is used and dependent variables at control surfaces are reconstructed based on gradients which are calculated using Green–Gauss theorem. For a physical time marching, a time derivative in the momentum equation is replaced with a second order three-point backward difference formula. Since the scheme is stable regardless of the physical time step size, the physical time step can be increased arbitrary provided that the variation of the flow field in time can be accurately resolved by the second order difference formula.

The interactions of vorticity fields with solid boundaries have been investigated related to flow induced vibration or noise generation. Among those vorticity field and body interactions, the cases of a body in the wake of another body are frequent. For instance, tubes in the wake of upstream tubes in a heat exchanger or rotor blades passing through the wakes of stator blades can be regarded as the case of a body in the wake of another body. Gursul and Rockwell [3] carried out an experimental study for the vortex street impinging upon an elliptical leading edge. During the interactions, the structures of vortices are exposed to rapid distortions near the leading edge. Furthermore, the vortices may be severed and a secondary vortex can be formed by boundary layer separation. So the flow field may be very complicated. Although the flow visualization results provide valuable information to understand evolution of the vorticity field, it is not clear how the distortion of a streakline or timeline pattern is related to the distortion of a vorticity field. Kaya and Kaykayoglu [4] used a discrete vortex method to simulate the previous experiments. However, the discrete vortex method cannot include some important features such as interaction of the incident vorticity field with the boundary layer vorticity.

Navier–Stokes calculations can be helpful to analyse such a complicated flow structure by providing details of flow structure at any location, which cannot be furnished accurately in experiments. As an instance, an instantaneous vorticity field should be calculated based on a finite difference formula based on the measured velocity field in the experiment [3]. Although the measurement stencil is suitable to resolve the velocity field, it does not imply that the stencil is fine enough to use the numerical differentiation to obtain accurate vorticity field. Using clustered grid along the path of the vortices, accurate vorticity fields at any desired instances can be provided by Navier–Stokes calculations on unstructured grids.

Qualities of structured grids around multi-bodies depend on the arrangement and configurations of the bodies. Additionally it is crucial to maintain the grid resolution along the path of the vortices for the flow fields containing the convecting vortices. Therefore, it may cause difficulties for structured grids if the incident vortex street is shifted from the centreline of the downstream body. In fact, these arrangements are as the experiments are carried out [3]. Due to its inherent flexibility in the grid generation, the unstructured grid method provides efficient way to analyse these kinds of flow fields. For unstructured grids, the arrangement and configurations of bodies do not cause any difficulty and the clustering to arbitrary locations can be achieved by simply assigning a few source points at the desired locations in the background grid.

2. NUMERICAL METHOD

In this study, the developed steady solver [5] is expanded to calculate an unsteady flow. The governing equations are the time-dependent Navier–Stokes equations for incompressible flow.

For an arbitrary control volume, Ω, whose control surface is $\partial\Omega$, the governing equations can be written as an integral form as follows:

$$\frac{\partial}{\partial t}\int_{\Omega} Q\,\mathrm{d}V + \oint_{\partial\Omega} F_{\mathrm{inv}}\,\mathrm{d}S - \oint_{\partial\Omega} F_{\mathrm{vis}}\,\mathrm{d}S = 0 \tag{1}$$

For a two-dimensional case,

$$Q = \begin{bmatrix} 0 \\ u \\ v \end{bmatrix}, \quad F_{\mathrm{inv}} = \begin{bmatrix} \Theta \\ u\Theta + pn_x \\ v\Theta + pn_y \end{bmatrix}, \quad F_{\mathrm{vis}} = \begin{bmatrix} 0 \\ \tau_{xx}n_x + \tau_{xy}n_y \\ \tau_{yx}n_x + \tau_{yy}n_y \end{bmatrix}, \quad \Theta = un_x + vn_y \tag{2}$$

A node-based finite volume method is used to discretize the governing equations spatially where all the dependent variables are defined at vertices of the grid. A non-overlapping control volume surrounding each node is defined by control surface portions that are connecting the centroid of the element to the midpoint of boundary of the element.

Time derivatives in the momentum equations are replaced with a second order, three-point, backward difference formula.

$$\left.\frac{\partial u}{\partial t}\right|^n \approx \frac{3u^n - 4u^{n-1} + u^{n-2}}{2\Delta t} \tag{3}$$

Then the discretized equations for the dependent variables of ith node at nth time step can be written as follows.

$$\frac{1.5V_i}{\Delta t}\begin{bmatrix} 0 \\ u_i^n \\ v_i^n \end{bmatrix} + R_i(p^n, u^n, v^n) = \frac{V_i}{\Delta t}\begin{bmatrix} 0 \\ 2u_i^{n-1} - 0.5u_i^{n-2} \\ 2v_i^{n-1} - 0.5v_i^{n-2} \end{bmatrix} \tag{4}$$

where V_i is the size of the control volume of the ith node. The $R_i(p^n, u^n, v^n)$ is the residual at the ith node calculated by the numerical fluxes through the control surface. The numerical fluxes are calculated based on the dependent variables at nth time step. To couple the pressure and velocity fields, the artificial compressibility with respect to the pseudotime τ is introduced as follows.

$$V_i\frac{\partial}{\partial\tau}\begin{bmatrix} \tilde{p}_i \\ \tilde{u}_i \\ \tilde{v}_i \end{bmatrix} + \frac{1.5V_i}{\Delta t}\begin{bmatrix} 0 \\ \tilde{u}_i \\ \tilde{v}_i \end{bmatrix} + \tilde{R}_i(\tilde{p}, \tilde{u}, \tilde{v}) = \frac{V_i}{\Delta t}\begin{bmatrix} 0 \\ 2u^{n-1} - 0.5u^{n-2} \\ 2v^{n-1} - 0.5v^{n-2} \end{bmatrix} \tag{5}$$

where $\tilde{R}_i(\tilde{p}, \tilde{u}, \tilde{v})$ is the residual calculated based on $(\tilde{p}, \tilde{u}, \tilde{v})$ with the modification in the continuity equation due to the artificial compressibility,

$$\tilde{F}_{\mathrm{inv}} = \begin{bmatrix} \beta\tilde{\Theta} \\ \tilde{u}\tilde{\Theta} + \tilde{p}n_x \\ \tilde{v}\tilde{\Theta} + \tilde{p}n_y \end{bmatrix}, \quad \tilde{\Theta} = \tilde{u}n_x + \tilde{v}n_y \tag{6}$$

where β is the artificial compressibility parameter.

Subiteration is carried out to get steady state solution of $(\tilde{p}, \tilde{u}, \tilde{v})$ with respect to the pseudotime τ. Once the steady solution is obtained, the flow field at nth time step (p^n, u^n, v^n) in Equation (4) is replaced with the intermediate flow field $(\tilde{p}, \tilde{u}, \tilde{v})$. For the subiteration with respect to the pseudotime, τ, an implicit time marching based on linearized Euler backward method with the local time stepping is used [5]. For $m+1$th pseudotime step, Euler backward difference can be written as follows.

$$\frac{V_i}{\Delta\tau}\begin{bmatrix} \tilde{p}^{m+1}-\tilde{p}^m \\ \tilde{u}^{m+1}-\tilde{u}^m \\ \tilde{v}^{m+1}-\tilde{v}^m \end{bmatrix} + \frac{1.5V_i}{\Delta t}\begin{bmatrix} 0 \\ \tilde{u}^{m+1} \\ \tilde{v}^{m+1} \end{bmatrix} + \tilde{R}(\tilde{p}^{m+1}, \tilde{u}^{m+1}, \tilde{v}^{m+1}) = \frac{V_i}{\Delta t}\begin{bmatrix} 0 \\ 2u^{n-1}-0.5u^{n-2} \\ 2v^{n-1}-0.5v^{n-2} \end{bmatrix} \tag{7}$$

Equation (7) can be linearized as follows.

$$\left(\begin{bmatrix} \frac{V_i}{\Delta\tau} & 0 & 0 \\ 0 & V_i\left(\frac{1}{\Delta\tau}+\frac{1.5}{\Delta t}\right) & 0 \\ 0 & 0 & V_i\left(\frac{1}{\Delta\tau}+\frac{1.5}{\Delta t}\right) \end{bmatrix} + \frac{\partial\tilde{R}(\tilde{p}^m, \tilde{u}^m, \tilde{v}^m)}{\partial(\tilde{p}^m, \tilde{u}^m, \tilde{v}^m)}\right)\begin{bmatrix} \tilde{p}^{m+1}-\tilde{p}^m \\ \tilde{u}^{m+1}-\tilde{u}^m \\ \tilde{v}^{m+1}-\tilde{v}^m \end{bmatrix}$$

$$= -\tilde{R}(\tilde{p}^m, \tilde{u}^m, \tilde{v}^m) - \begin{bmatrix} 0 \\ \frac{V_i}{\Delta t}(1.5\tilde{u}^m - 2u^{n-1} + 0.5u^{n-2}) \\ \frac{V_i}{\Delta t}(1.5\tilde{v}^m - 2v^{n-1} + 0.5v^{n-2}) \end{bmatrix} \tag{8}$$

where $\partial\tilde{R}(\tilde{p}^m, \tilde{u}^m, \tilde{v}^m)/\partial(\tilde{p}^m, \tilde{u}^m, \tilde{v}^m)$ is the Jacobian matrix of the residual vector with respect to the dependent variable vector. Although the scheme is stable at very large value of the local Courant number based on the pseudotime step size, $\Delta\tau$, there is an optimal value for the total calculation time due to the fact that the large value of the local Courant number reduces diagonal dominance of the Jacobian matrix. A typical value of the local Courant number used in this study is 200. Since the physical time step, Δt, does not cause any instability related to the Courant number, it can be increased arbitrary provided that the physical time step, Δt, is small enough to resolve the variation of the flow field in time by the second order three-point backward difference formula.

Inviscid flux through each control surface portion assigned to each edge is calculated using Roe's flux difference splitting method [6].

$$F_{\text{inv}} = \frac{1}{2}[F(Q_{\text{L}}) + F(Q_{\text{R}})] - \frac{1}{2}|\hat{A}|(Q_{\text{R}} - Q_{\text{L}}) \tag{9}$$

where Q_{L} and Q_{R} are dependent variable vectors at the left and right sides of the control surface portion. To obtain a higher order accuracy, the Q_{L} and Q_{R} are reconstructed based

on the Taylor series expansion. Using the Green–Gauss theorem, the gradients in the Taylor series expansion are calculated as follows.

$$\nabla Q \approx \frac{1}{\text{Volume}} \oint_{\partial\Omega} Q\mathbf{n}\,\mathrm{d}S \tag{10}$$

To calculate viscous fluxes, the gradients of velocities at each element are calculated using the Green–Gauss theorem again. However, for these gradients of velocities, the integration in Equation (10) is carried out along the boundary of the element instead of the control surface. Based on the gradients of velocities at each element and control surface potions, the viscous flux contributions to nodes of the element are calculated.

Contributions of viscous fluxes to the Jacobian matrix are calculated exactly. However, some approximations are made for contributions of inviscid fluxes to the Jacobian matrix to guarantee diagonal dominance of the matrix and to reduce memory requirement. Since exact linearization of Roe's fluxes can cause loss of the diagonal dominance, the Roe's matrix, $|\hat{A}|$, is taken as a frozen matrix during the Jacobian calculation [7]. To save memory requirements for the Jacobian matrix, the effect of data reconstruction of Q_L and Q_R on the Jacobian matrix is ignored so that Q_L and Q_R are taken as the dependent variable vectors at the nodes. This approximation reduces the number of non-zero coefficients in the Jacobian matrix significantly. Because the most part of the memory is used to save the non-zero coefficients of the Jacobian matrix, this approximation is crucial to reduce the memory requirement. Only non-zero coefficients of the Jacobian matrix are saved and the matrix structure is given using the compressed row storage method [8].

On a body boundary, no slip condition is applied. The pressure at the body boundary node is calculated based on a residual at the boundary node. To define a closed control volume for the body boundary node, the control surface portion on the body surface should be added. However, the contribution of the flux through that control surface portion to the residual of continuity equation vanishes due to the zero normal velocity at the body boundary. Dependent variables at inflow boundary are fixed. At outflow boundary, dependent variables are extrapolated from dependent variables at neighbouring inside nodes.

3. RESULTS AND DISCUSSIONS

3.1. Flow over a circular cylinder at a Reynolds number of 200

To validate the code, unsteady laminar flow over a circular cylinder at Reynolds number of 200 is calculated. The Reynolds number is based on the free stream velocity and the diameter of the cylinder. An unstructured grid is shown in Figure 1. The grid contains 26 578 nodes and 52 934 triangles. On the circular cylinder, 140 nodes are distributed. Far field boundary is located at 20 diameters behind the cylinder. On the far field boundary 82 nodes are distributed. For the viscous grid, the first layer height is 0.001 and layer heights are increased by a geometric series with a factor of 1.15. The physical time step, Δt, is 0.05. Pseudotime step, $\Delta\tau$, of each node is calculated so that the local Courant number of each cell is 200. The artificial compressibility parameter, β, is 100. From a free-stream condition, the flow is started impulsively.

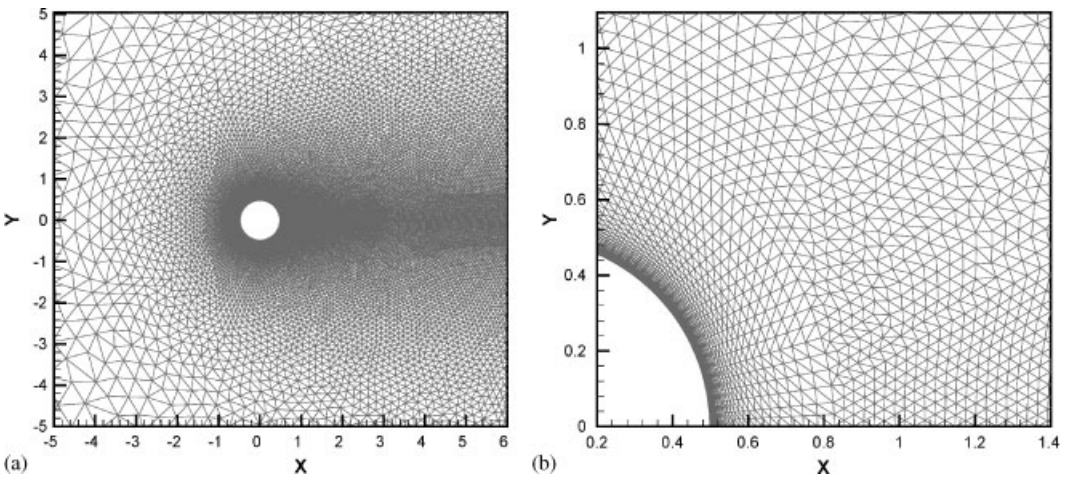

Figure 1. Unstructured grid for flow around a circular cylinder.

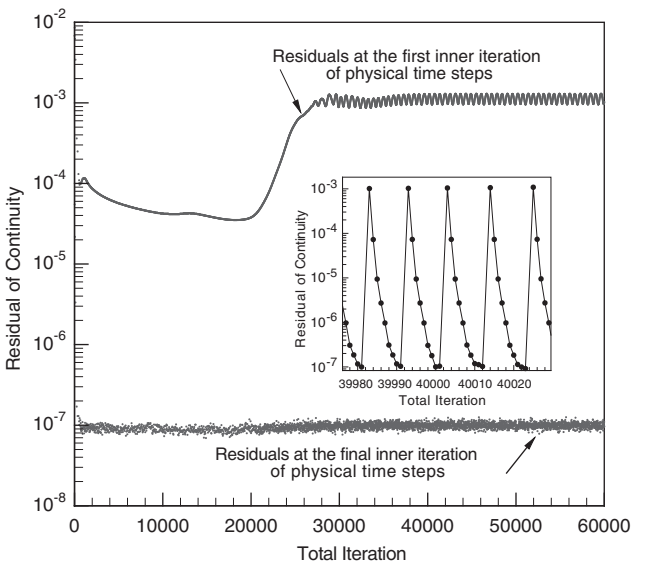

Figure 2. Convergence history of residual of continuity equation.

In Figure 2, the behaviour of continuity equation residuals are shown as a function of iteration step. After the asymmetric wake is fully developed, about ten pseudotime step iterations are required for each physical time step to reduce the continuity equation residuals by four digits. In Figure 2, the residuals at the first and the final pseudotime steps are indicated for all physical time steps. The behaviour of the residuals of the first pseudotime steps is very similar to the variation of the drag with respect to time as shown later. At the initial stage,

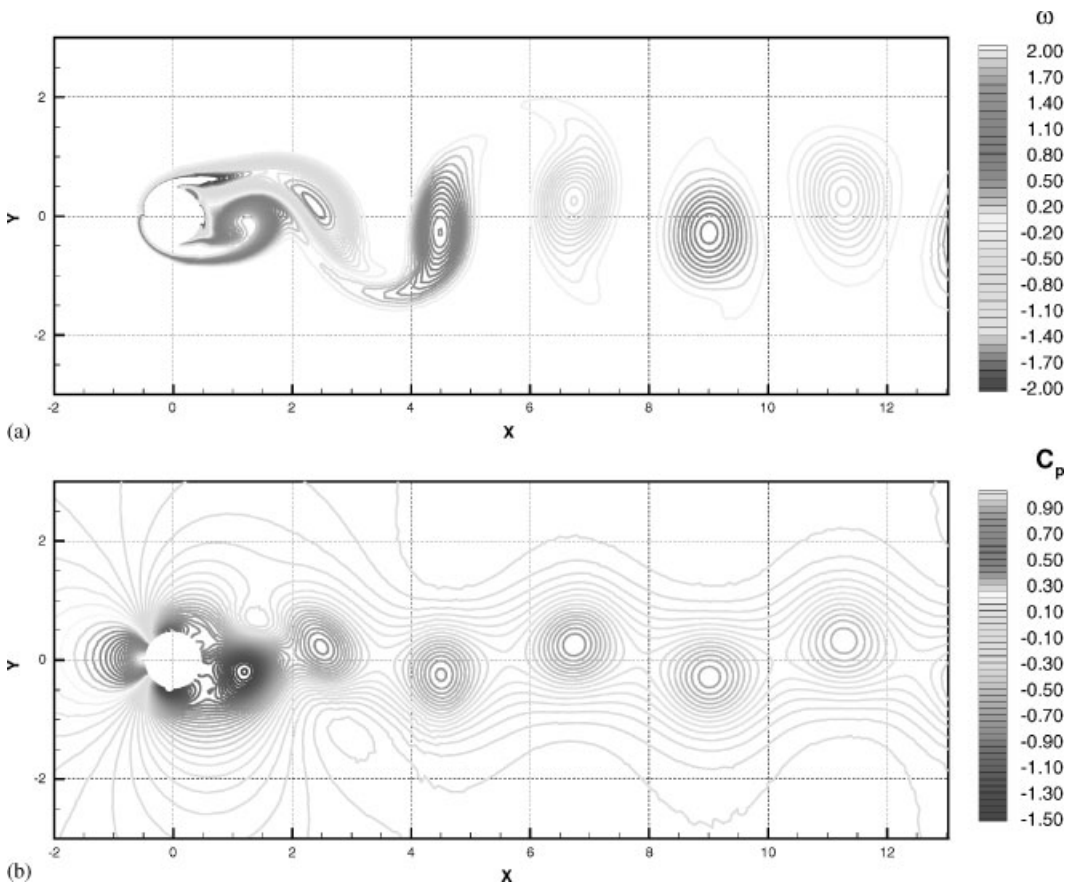

Figure 3. Instantaneous vorticity and pressure contours of flow over a circular cylinder at a Reynolds number of 200.

there is abrupt change in the flow field due to the acceleration from the rest and it causes high level of residuals. When two symmetric vortices are located behind the cylinder, the flow field varies slowly and the residuals of the first pseudotime iterations are also small. Although the residuals of the first pseudotime iterations increase as vortices are shed, the residuals of the final pseudotime iterations can be decreased to the similar level with one additional pseudotime iteration.

Figure 3 shows instantaneous vorticity and pressure contours. Vorticity contours show the evolution of each vortex as it moves downstream clearly. Compared with recent numerical results of Kiris [1], the centres of vortices are more closely aligned with the centreline of the cylinder and the shapes of the contours are closer to concentric circles.

Time histories of drag and lift coefficients are shown in Figure 4. The overall configurations of time histories are very similar to that of the previous calculation [1] except the non-dimensional time when the asymmetric wake starts to develop. For the periodic cycle, the drag and lift coefficients are: $C_D = 1.303 \pm 0.0357$ and $C_L = \pm 0.621$. The Strouhal number

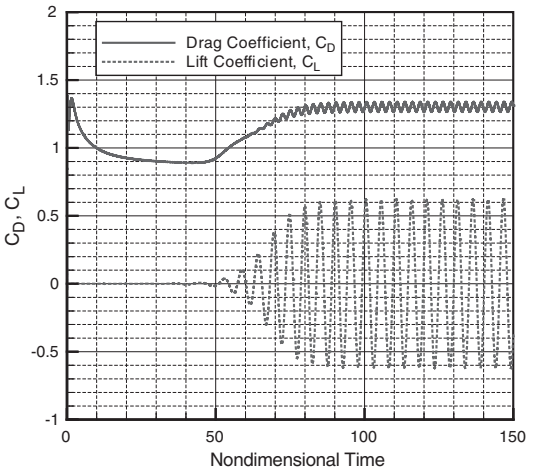

Figure 4. Time history of drag and lift coefficients of flow over a circular cylinder at a Reynolds number of 200.

Table I. Drag and lift coefficients and Strouhal number of flow over a circular cylinder at a Reynolds number of 200.

		C_D	C_L	St
Present		1.303 ± 0.0357	± 0.621	0.194
Experiments	Wille (1960)	1.30	—	—
	Kovasznay (1949)	—	—	0.19
Numeric	Kiris (2001)	1.27 ± 0.04	± 0.67	0.184
	Farrant (2000)	1.36	± 0.71	0.196
	Slaouti (1992)	—	± 0.62	0.196

Table II. Variations of drag and lift coefficients and Strouhal number with respect to physical time step size, Δt.

Δt	C_D/C_D^*	C_L/C_L^*	St/St^*
0.025	1.0003	1.0002	1.0008
0.050*	1.0	1.0	1.0
0.100	0.9981	0.9955	0.9947
0.200	0.9962	0.9848	0.9776
0.300	0.9895	0.9404	0.9506
0.400	0.9754	0.8922	0.9165

*Reference value.

is 0.194. In Table I, present results are compared with experimental results [9, 10] and other calculations [1, 11, 12]. The present results are in good agreement with experimental and other numerical results.

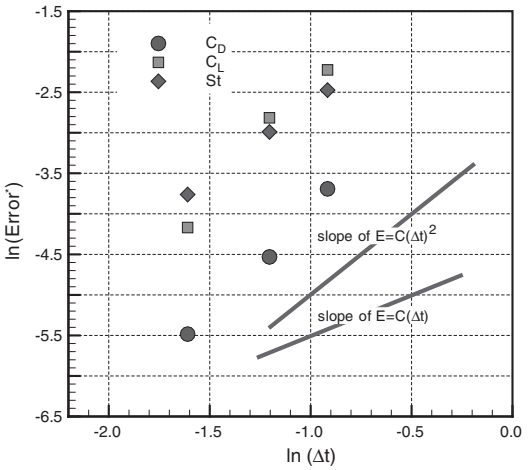

Figure 5. Variation of estimated error with respect to physical time step size, Δt.

To test the effects of numerical parameters on the final results, several cases are calculated with variations on the parameters including the physical time step size, Δt, total number of nodes, N_{node}, artificial compressibility, β and computational domain size, D/d_{cylinder}. In Table II, effects of the physical time step size, Δt, on the drag and lift coefficients and Strouhal number are indicated. The physical time step size, Δt, is varied from 0.025 to 0.4 which correspond to 205 and 14 time steps per calculated period, respectively. Even though the physical time step size, Δt, is increased from 0.05 to 0.2, the changes in the results are less than 2.3%. In Figure 5, the behaviour of the estimated errors with respect to the physical time step size, Δt, is shown. The estimated errors are defined as the deviations from the results at $\Delta t = 0.025$. It can be seen that the slopes of the variations in a log–log diagram are very close to the slope of a second-order scheme. In Table III, variations of the results are summarized with respect to the grid size, the artificial compressibility parameter, β, and the computational domain size. The table shows satisfactory behaviour of the results to convince the fact that the present grid and computational domain size are fine and large enough to get converged results. However, the lift coefficient show slight dependency on the artificial compressibility parameter, β, so that the lift is increased by 3.6% and decreased by 2.4% as the artificial compressibility parameter, β, is changed from 100 to 50 and 150.

3.2. Interaction of a Karman vortex street with an elliptical leading edge

Using the developed unsteady code, the interactions of the Karman vortex streets with an elliptical leading edge are simulated which has been investigated experimentally by Gursul and Rockwell [3]. The incident vortex streets are generated by upstream circular cylinders of two different diameters: $D_{\text{cylinder}}/D_{\text{body}} = 0.4$ and 0.24, where D_{body} is the thickness of the body. Large and small cylinders correspond to large-scale and small-scale vortex streets, respectively. The centres of the upstream cylinders are located at $L/D_{\text{body}} = 6$ and $\varepsilon/D_{\text{body}} = 0.4$, where L is the distance between the centre of the upstream cylinder and the leading edge of the body

Table III. Variations of drag and lift coefficients and Strouhal number with respect to total nodes numbers, artificial compressibility parameter and computation domain size.

	C_D/C_D^*	C_L/C_L^*	St/St^*
N_{node}		Variations with respect to numbers of total nodes	
8475	1.025	1.0354	0.9865
14816	0.9945	0.9910	0.9927
26578*	1.0	1.0	1.0
β		Variations with respect to artificial compressibility parameter, β	
50.	1.011	1.036	1.003
100.*	1.0	1.0	1.0
150.	0.992	0.976	0.997
$D/d_{cylinder}$		Variations with respect to computational domain size $D/d_{cylinder}$	
10.	1.015	1.033	1.004
20.*	1.0	1.0	1.0
40.	0.995	0.993	0.996

*Reference value.

and ε is the distance between the centreline of the upstream cylinder and centreline of the body. The ratio of major to minor axis of the elliptic leading edge is 5 : 1.

The Reynolds number based on the thickness of the body is 2500 and it is similar to that of the experiment [3]. In the experiments, the incoming vortex street is generated using an upstream plate instead of a cylinder and the Reynolds number based on the plate thickness was in the range 309–619. Although the upstream cylinders seem to be large to guarantee laminar wake, the diameters of upstream cylinders are decided to generate vortex streets which have similar distances between two neighbouring vortices as explained later.

3.2.1. Case A: Interaction of a large-scale vortex street. In Figure 6, an unstructured grid around an upstream cylinder and a downstream body is shown. It contains 108 356 nodes and 215 681 triangles. First, a background grid is assigned by solving the Poisson equation on a simple Cartesian grid with source distribution that controls grid size throughout the whole domain. Sources are distributed at the centre of the upstream cylinder, leading edge of the downstream body and expected path of the vortices. Then nodes are distributed on the boundary surface so that the spacing between the nodes on the boundaries complies with the required grid size at the location. Viscous grids are generated around the upstream cylinder and the body using the advancing layer method. For the rest of the domain, the advancing front method is used. Clustering to arbitrary locations with any desired grid size can be achieved simply by adjusting the locations and strengths of the source distribution.

In Figure 7, instantaneous vorticity and pressure contours are shown. Due to the effect of the downstream body, rapid distortions of vortices occur ahead of the leading edge. Near the leading edge, the vortices of counter-clockwise rotation move downward and collide with the leading edge of the body. Then the row of vortices of counter-clockwise rotation loses its identity as a row of vortices. In the vorticity contours, some vortices of counter-clockwise rotation can be identified after the collision. However, it can be seen from the pressure contours that the strength of the vortex diminishes immediately after the collision. Contrary

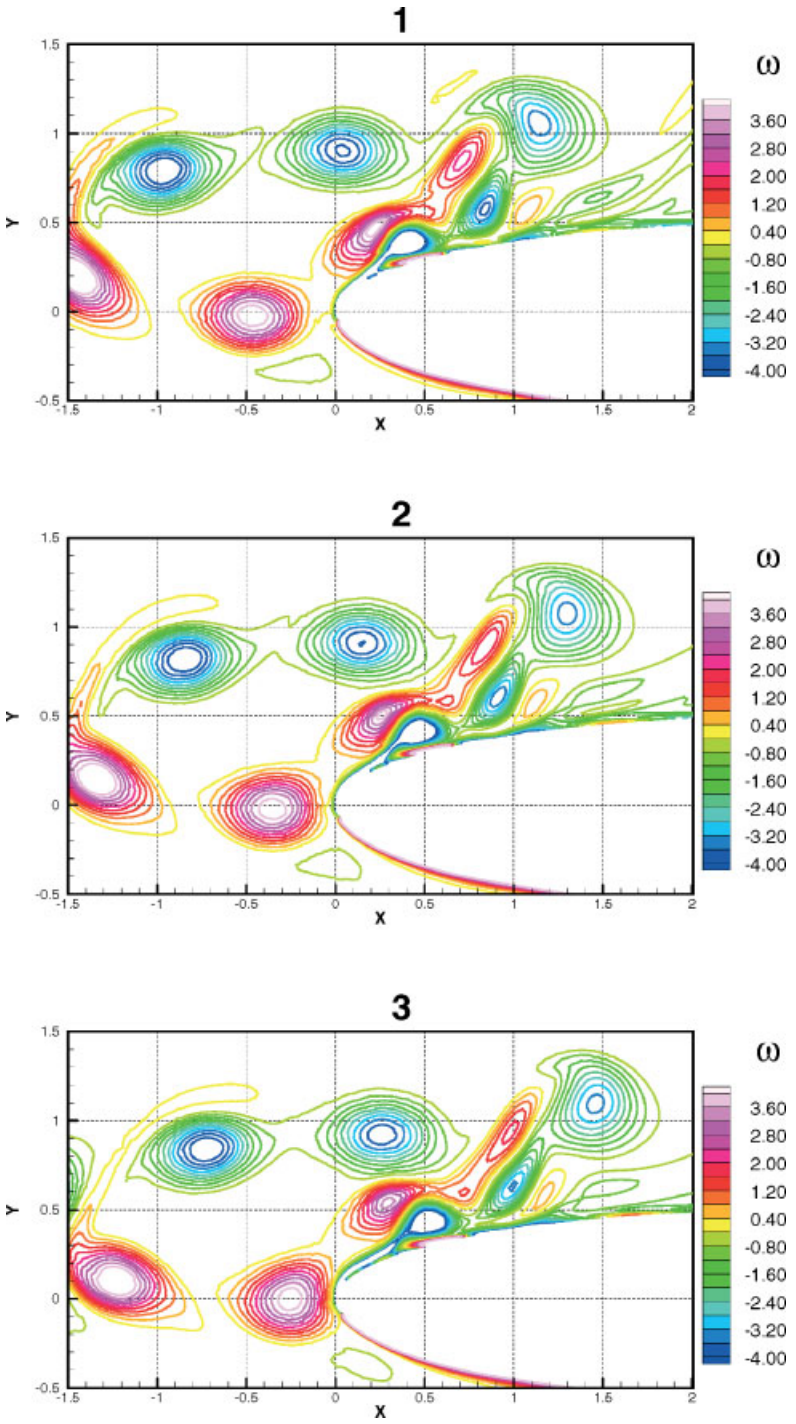

Plate 1.

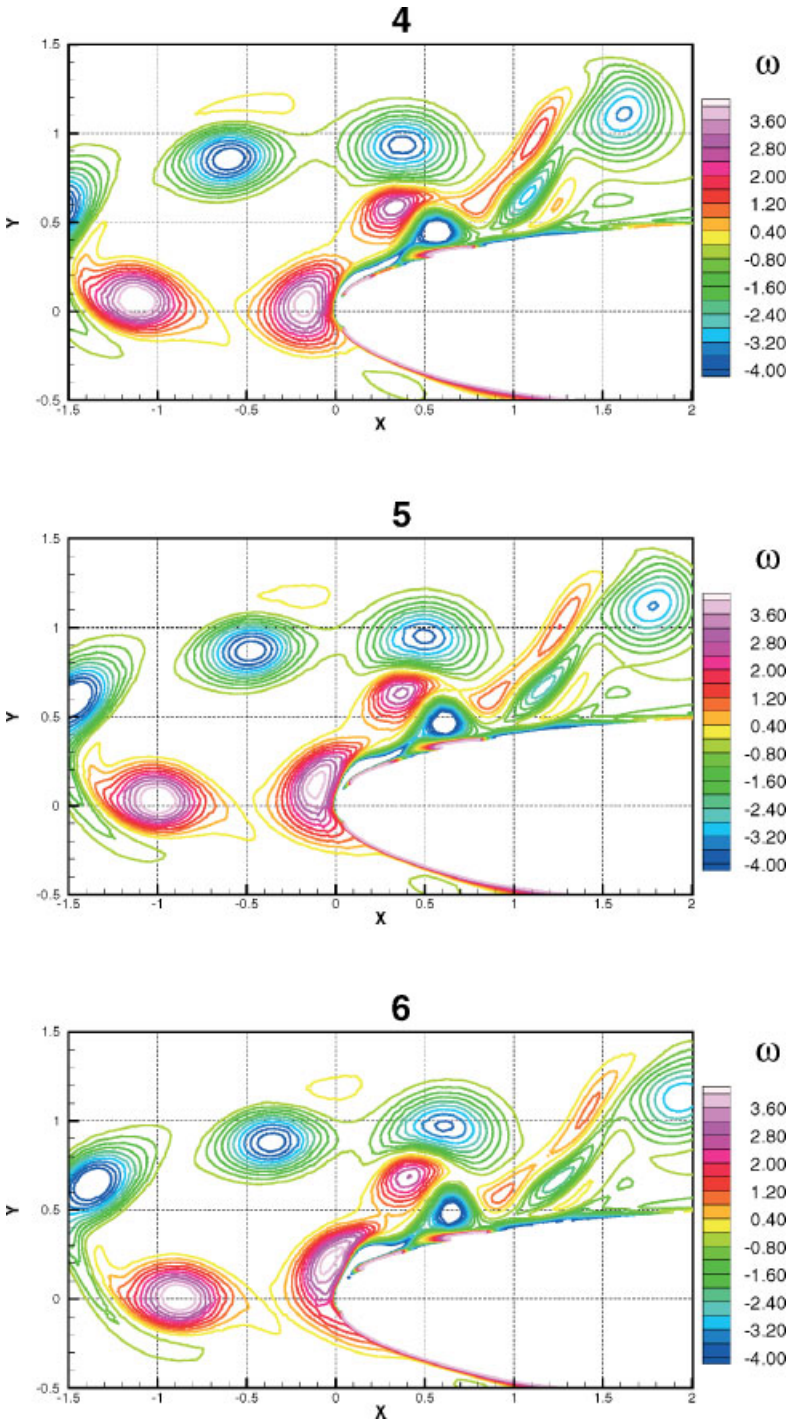

Plate 1.

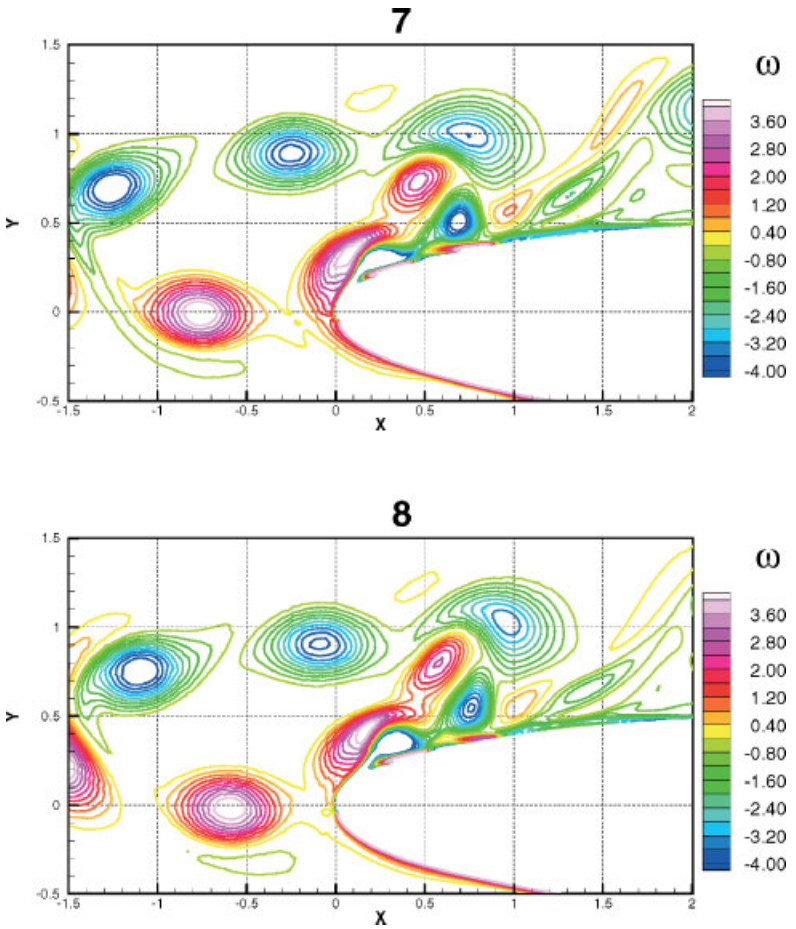

Plate 1. Eight instantaneous vorticity contours in one period of an interaction of a vortex street with an elliptical leading edge (large-scale vortex street).

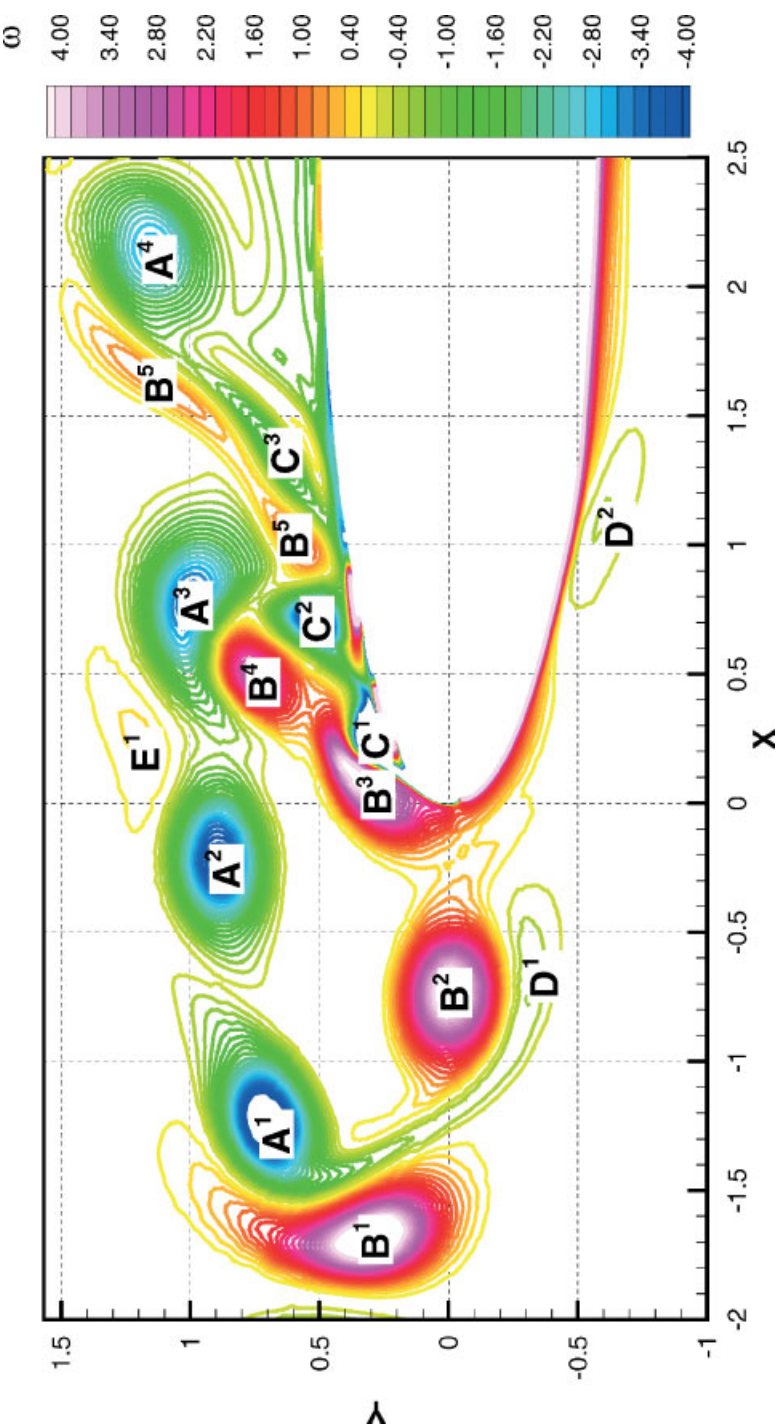

Plate 2. Categorizations of vortices in an instantaneous vorticity contours (large-scale vortex street).

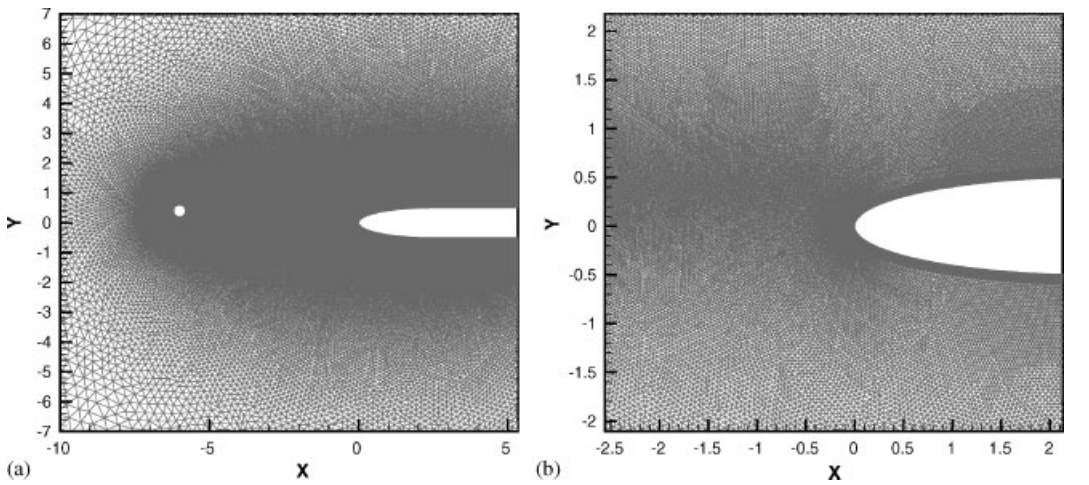

Figure 6. Unstructured grid for an interaction of Karman vortex street with an elliptical leading edge.

to the vortices of counter-clockwise rotation, the vortices of clockwise rotation move upward near the leading edge. Although the strengths of vortices are decreased after the interaction, the row of vortices of clockwise rotation maintains its identity clearly after the interaction.

In the experiments of Gursul [3], two different interaction types are observed when the centreline of the incoming vortex street is shifted from the centreline of the elliptical leading edge. For the cases where the incoming vortex street is small-scale, it is observed that two rows of vortices maintain their identities as rows of vortices throughout the interaction. However, as the scale of the incoming vortex street is increased, one row of vortices loses its identity as a row of vortices. The latter corresponds to the case where the ratio of the distance between neighbouring vortices in a row to the diameter of the after body is 1.62. Although it is not clear to compare the scale of incoming vortex street in the experiment and that of this calculation due to the difference in the vortex street generation, the distances between the neighbouring vortices in a row of the incoming vortex street are similar for both cases. However, the distance between the centrelines of vortex street and the elliptical leading edge is larger than the distance in the experiments, $\varepsilon/D_{\text{body}} = 0.16$.

After the interaction with the leading edge, the pressure distribution of the body surface is dominated by the row of vortices of clockwise rotation. In the vorticity contours, small vortices of clockwise rotation on the body surface can be seen. These are secondary vortices generated by boundary layer separation due to the existence of the vortex of counter-clockwise rotation near the body surface. The generation of the secondary vortex due to the separation can be seen clearly from the instantaneous velocity field in Figure 8. Due to the vortex of counter-clockwise rotation near the nose point, outward velocity component is induced near the wall. This outward velocity causes separation of the boundary layer near the nose point then the separation results in the generation of a secondary vortex of clockwise rotation. As the secondary vortex moves downstream, it becomes more circular in shape. The vortex near the body surface at $X \approx 0.6$ and $Y \approx 0.4$ in Figure 8 is a vortex that is shifted downstream from the nose point. However, this secondary vortex diffuses and eventually disappears as it moves further downstream due to the strong viscous effect of the boundary layer.

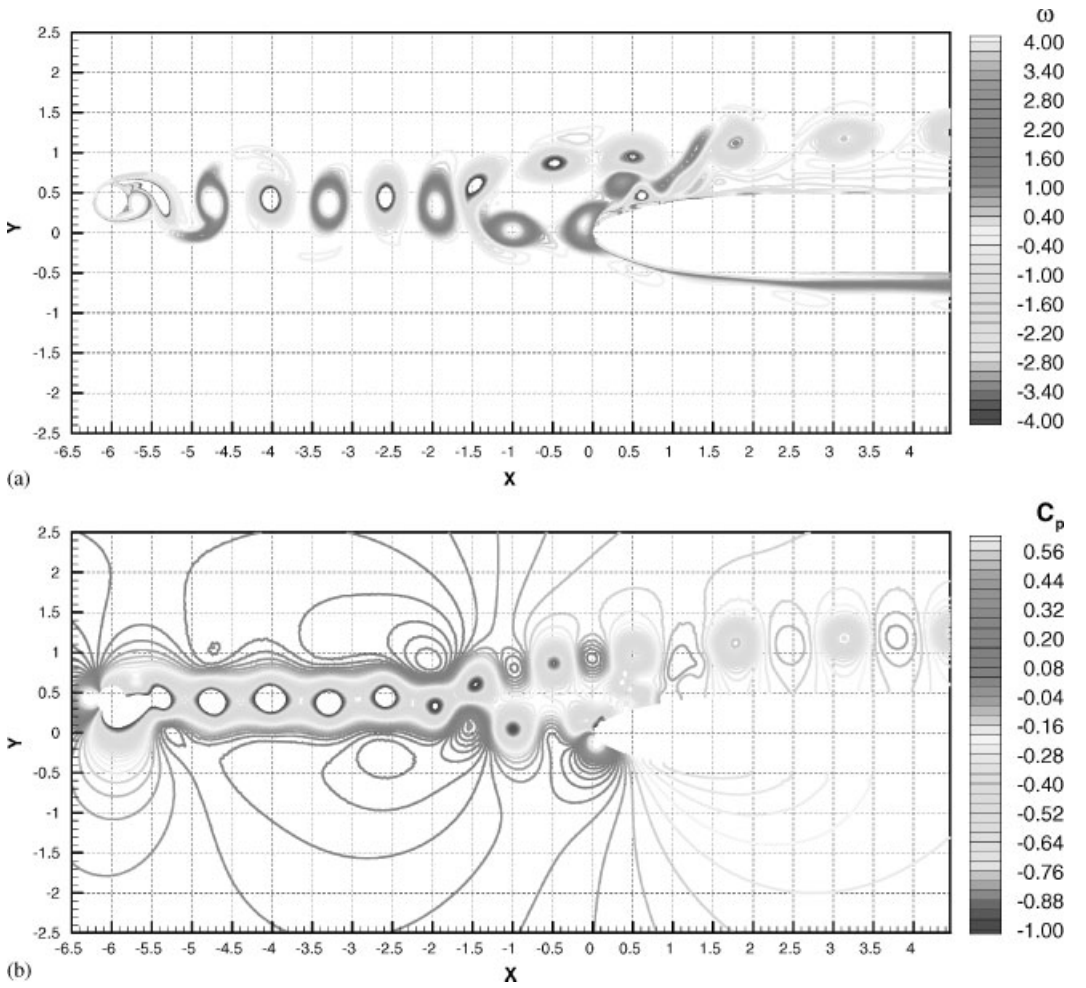

Figure 7. Instantaneous vorticity and pressure contours of an interaction of a vortex street with an elliptical leading edge (large-scale vortex street).

To show details of the interaction mechanism clearly, eight instantaneous vorticity contours in one period are shown in Plate 1 sequentially. By investigating evolutions of vortices in Plate 1, the origins of all vortices, which can be identified in Figure 7, may be clarified. After examination of the evolutions of vortices, all vortices are categorized according to their origin in Plate 2. As explained previously, the row of clockwise rotating vortices maintain its identity clearly throughout the interaction ($A^1 - A^2 - A^3 - A^4$). However, the row of counter-clockwise rotating vortices loses its identity during the interaction ($B^1 - B^2 - B^3 - B^4 - B^5$). The major contribution for the loss of the vortex strength comes from the interaction with the body surface (B^3), then the vortex is dissipated eventually by the strong viscous effect. A secondary vortex due to the boundary layer separation is generated (C^1) and moves downstream ($C^2 - C^3$). As the incoming vortices approach the leading edge, the convectional

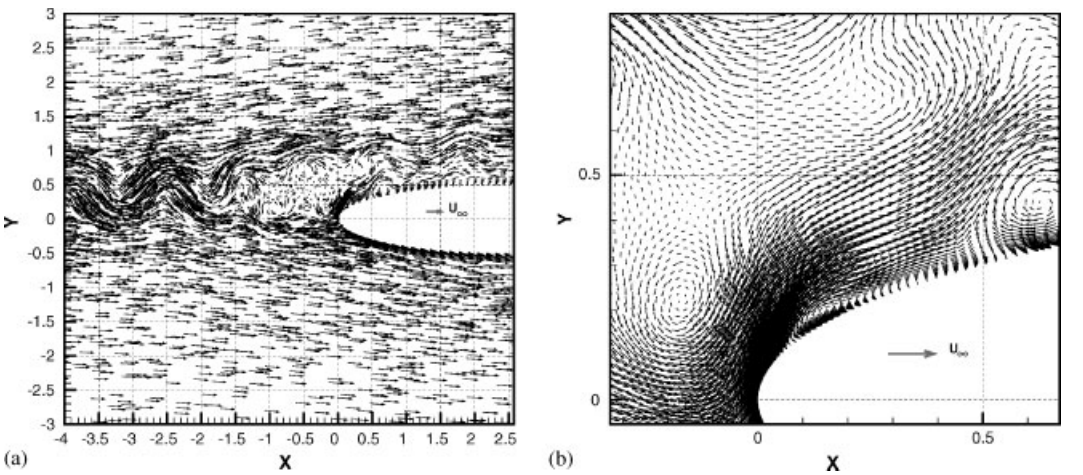

Figure 8. Instantaneous velocity field of an interaction of a vortex street with an elliptical leading edge (large-scale vortex street).

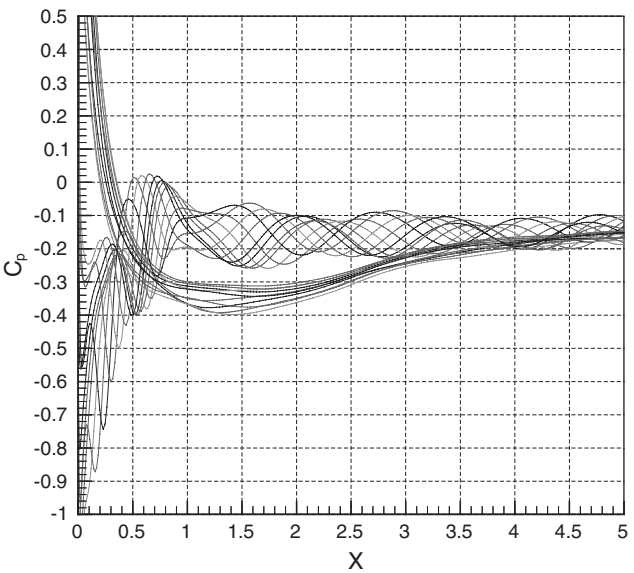

Figure 9. Fluctuation of pressure coefficients distribution on a body (large-scale vortex street).

velocities of the vortices are decreased. These decreases in the convectional velocities cause contact of neighbouring vortices and rapid distortion. During this distortion, small parts of vorticity are separated and move downstream (E^1, D^1, D^2).

In Figure 9, the fluctuations in the pressure distribution on the body surface are shown. As expected from the pressure contours in Figure 7, local minimums occur at the locations where

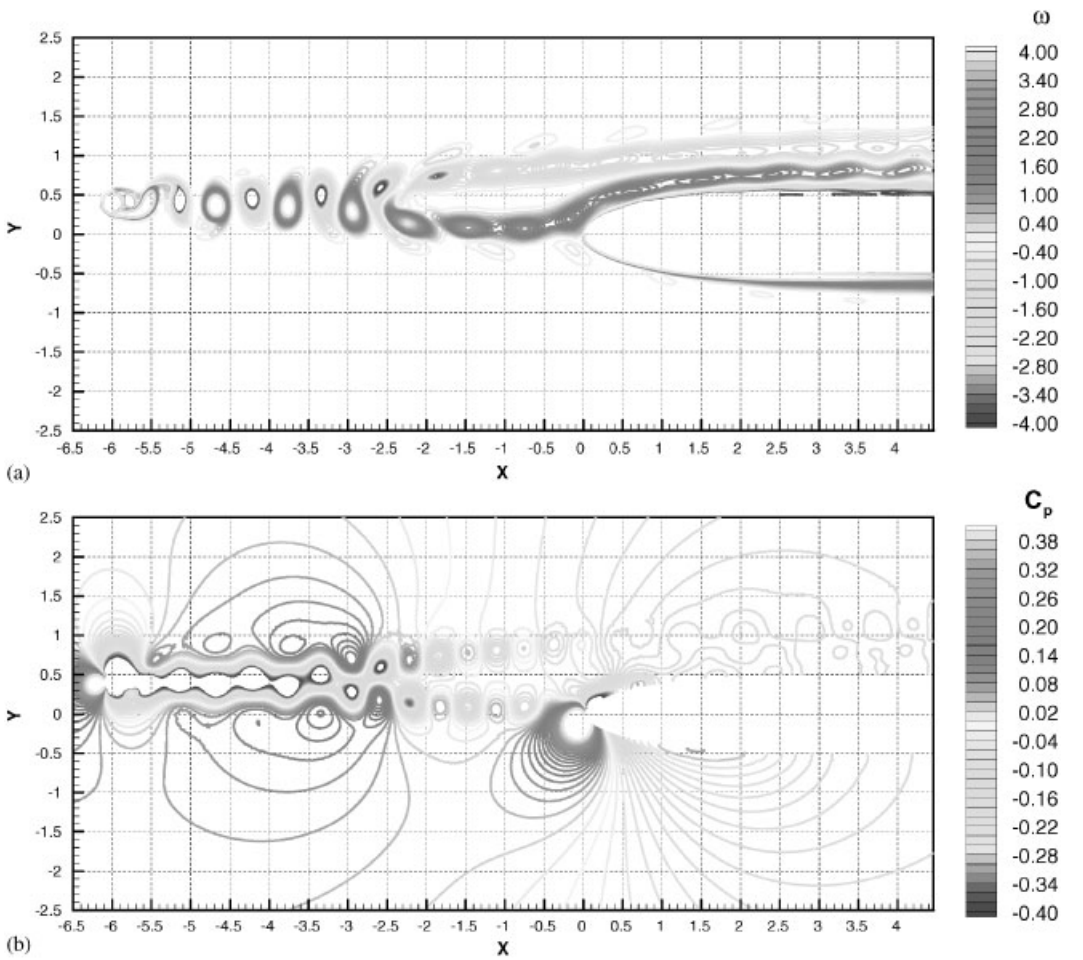

Figure 10. Instantaneous vorticity and pressure contours (small-scale vortex street).

the vortices of clockwise rotation are present. In the experiment of Gursul [3], it is observed that the amplitude of the fluctuation of the pressure distribution on the body surface does not decrease monotonically from the global maximum of the amplitude. The phenomenon can be observed in the present calculation also.

3.2.2. Case B: Interaction of a small-scale vortex street. To test the effect of the vortex street scale on the interaction, the diameter of the upstream cylinder is reduced to $0.24D_{\text{body}}$. Except the diameter of the upstream cylinder, all conditions are identical with the previous calculation. Instantaneous vorticity and pressure contours are shown in Figure 10. For this small-scale vortex street, it can be seen that two rows of vortices preserve their identities after the interaction with the leading edge. In the experiments of Gursul [3], it is observed that by reducing the incoming vortex scale, the characteristics of the interaction are changed in the same manner. For the small-scale vortex street whose ratio of distance between neighbouring

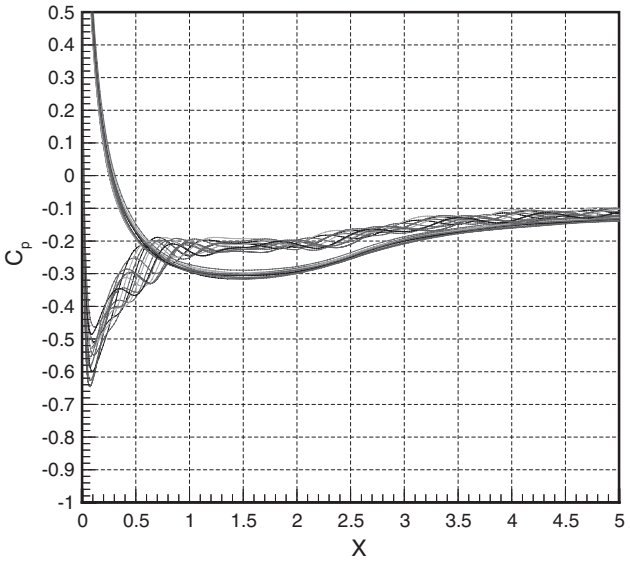

Figure 11. Fluctuation of pressure coefficients distribution on a body surface (small-scale vortex street).

vortices to the thickness of the body is 0.81, it is observed in the experiments that the rows of the incoming vortices maintain their identity throughout the interaction for all offset distances $\varepsilon/D_{\text{body}} = 0.16, 0.39, 0.59$.

For the small-scale vortex, the distortions of the vortices occur further upstream. The vortices of counter-clockwise rotation move downwards likewise the large-scale case. However, for the small-scale vortex, the vortices do not cross the centreline of the body. The centres of vortices contact with the body at a point slightly shifted from the centreline. After the collision, those vortices move along the body surface. Although the strengths of vortices of counter-clockwise rotation are decreased during the interaction, the fluctuations in the pressure distribution on the body surface are determined by the presence of the vortices of counter-clockwise rotation. The fluctuation of pressure distribution on the body surface is shown in Figure 11. Compared with the large-scale vortex street case, the amplitude of fluctuation is decreased significantly. Since the vortices of counter-clockwise rotation contact with the body surface at upper side of the body, the amplitude of the pressure fluctuation at $X = 0.5$ is close to the global maximum of the pressure fluctuation on the body surface whereas the maximum amplitude appears at $X = 0$ for the large-scale vortex street case.

4. CONCLUSIONS

An algorithm to solve the time accurate incompressible Navier–Stokes equations on an unstructured grid has been presented. The artificial compressibility method has been adapted successfully for the unsteady flow using the Roe's flux difference splitting method and the implicit method to accelerate the convergence with respect to the pseudotime. A second-order three-point backward difference has been used to approximate the physical time derivatives in the momentum equations and the physical time step size can be decided without considering

the stability. The iteration with respect to the pseudotime has been converged fast due to the implicit method with large local Courant number of 200.

As a validation of the developed unsteady code, the periodic vortex shedding from a circular cylinder at a Reynolds number of 200 has been calculated. Compared with other recent numerical results, the centre of each vortex is more closely aligned with the centreline of the cylinder and the shapes of the vorticity contours are closer to concentric circles. The calculated results have been compared with available experimental and numerical results. Good agreements have been achieved for Strouhal number and time history of the drag and lift coefficients. In the log–log diagram of the variation of the estimated errors with respect to the physical time step size, Δt, the scheme shows a behaviour which is expected for a second-order scheme in time.

Finally the code has been applied to analyse the interaction of the vortex street with the elliptical leading edge. Due to the flexibility of the unstructured grid, the clustering to the path of vortex street has been achieved readily, which is crucial to get accurate solutions. The details of the interaction mechanism have been analysed based on the sequence of evolutions of the vortices during one period. All the vortices identified in the instantaneous vorticity contours have been related to one of the three vortices: two incoming vortices of clockwise/counter-clockwise rotations and the secondary vortex generated by the flow separation. For the interaction of the large-scale vortex street, one row of vortices loses its identity as a row of vortices during the interaction. The incoming vortex near the leading edge induces boundary layer separation and the separation results in generation of the secondary vortex. However, for the small-scale vortex street, two rows of vortices preserve their identities after the interaction with the leading edge. These different types of interaction are in accordance with the observation in the experiments of Gursul [3]. For the amplitudes of the pressure fluctuations on the body surface, it is observed that the amplitudes do not decrease monotonically from the global maximum of the fluctuation amplitude. These tendencies are in agreement with the experimental results also.

REFERENCES

1. Kiris C, Kwak DC. Numerical solution of incompressible Navier–Stokes equations using a fractional-step approach. *Computers & Fluids* 2001; **30**:829–851.
2. Rogers SE, Kwak DC, Kiris C. Steady and unsteady solutions of the incompressible Navier–Stokes Equations. *AIAA Journal* 1991; **29**(4):603–610.
3. Gursul I, Rockwell D. Vortex street impinging upon an elliptical leading edge. *Journal of Fluid Mechanics* 1990; **211**:211–242.
4. Kaya MO, Kaykayoglu CR. Numerical simulation of a self-sustained wake-edge interaction. *Journal of Fluids and Structures* 1996; **10**:215–236.
5. Shin S, Ragab SA. RANS computations of tip clearance flow in a compressor cascade using an unstructured grid, *AIAA 2001-2999*, 2001.
6. Taylor LK, Whitfield DL. Unsteady three-dimensional incompressible Euler and Navier–Stokes solver for stationary and dynamic grids, *AIAA 91-1650*, 1991.
7. Anderson WK, Rausch RD, Bonhaus DL. Implicit/multigrid algorithms for incompressible turbulent flow on unstructured grids, *AIAA 95-1704*, 1995.
8. Wang M, Sheu T. On a compact mixed order finite element for solving the three-dimensional incompressible Navier–Stokes equations. *International Journal for Numerical Methods in Fluids* 1997; **25**(5):513–522.
9. Wille R. Karman vortex streets. *Advances in Applied Mechanics* 1960; **6**:273–281.
10. Kovaaznay LSG. Hot-wire investigation of the wake behind cylinders at low Reynolds numbers. *Proceedings of the Royal Society* 1949; **198**:174–190.
11. Farrant T, Tan M, Price WG. A cell boundary element method applied to laminar vortex-shedding from arrays of cylinders in various arrangements. *Journal of Fluids and Structures* 2000; **14**:375–402.
12. Slaouti A, Stansby PK. Flow around two circular cylinders by the random vortex method. *Journal of Fluids and Structures* 1992; **6**:641–670.

